Supplementary Information: Hierarchical defect-induced condensation in active nematics

Timo Krüger[a], **Ivan Maryshev**[a], **and Erwin Frey**[a,b⊠]

[a]Arnold Sommerfeld Center for Theoretical Physics (ASC) and Center for NanoScience (CeNS), Department of Physics, Ludwig-Maximilians-Universität München, Theresienstrasse 37, 80333 Munich, Germany
[b]Max Planck School Matter to Life, Hofgartenstraße 8, 80539 Munich, Germany

Correspondence: *frey@lmu.de*

Supplementary Note 1: WASP simulation method

In this section we provide a brief summary of the agent-based simulations. The focus will be on the aspects most relevant for the current study. For a detailed description of the WASP simulation setup, please refer to the supplemental materials of Refs. ([1], [2]).

In the agent-based simulations, we consider M polymers moving on a flat substrate (in two spatial dimensions). Each polymer n consist of N spherical joints j which are located at a positions $\mathbf{r}_j^{(n)}$ (with $j \in \{0, 1, \ldots, N-1\}$, where the polymer tip is denoted by $j = 0$). The direction of a polymer's tip is denoted by $\mathbf{u}_0^{(n)}$ and its motion is described by:

$$\partial_t \mathbf{r}_0^{(n)} = v^{(n)} \mathbf{u}_0^{(n)} - \mathbf{F}_{\text{rep}} = v^{(n)} \begin{pmatrix} \cos\theta_0^{(n)} \\ \sin\theta_0^{(n)} \end{pmatrix} - \mathbf{F}_{\text{rep}}. \tag{1}$$

Here $\mathbf{F}_{\text{rep}}$ describes a weak repulsion force (see Eq. (7)) acting on a polymer head while in contact with the contour of another polymer. $\theta_0^{(n)}$ denotes the orientation of a polymer and $v^{(n)}$ its free speed. For this study, the speed of each polymer was chosen at random from a continuous uniform distribution in the interval $[0.75, 1]v_0$, where v_0 denotes the maximal velocity of a free polymer (see section S5 for further details on this velocity dispersion).

The orientation of a polymer's head evolves in time according to

$$\partial_t \theta_0^{(n)} = -\frac{\delta \tilde{H}_0^{(n)}}{\delta \theta_0^{(n)}} + \sqrt{\frac{2v^{(n)}}{L_p}} \xi, \tag{2}$$

where ξ is random white noise with zero mean and unit variance with the magnitude of the noise given by the prefactor. This implies that individual polymers perform a persistent random walk with a path persistence length of L_p. $\tilde{H}_0^{(n)}$ sets the—in this study purely nematic—torque caused by interactions with other polymers.

Before we come to a description of $\tilde{H}_0^{(n)}$, it will proof useful to introduce several other quantities. The first is the distance vector

$$\Delta \mathbf{r}_{nm} = \left(\mathbf{r}_0^{(n)} - \mathbf{r}^{(m)} \right)_{\text{shDist}}. \tag{3}$$

This vector connects the tip of a polymer n with the position of an adjacent polymer's (denoted by m) contour that has the shortest possible distance. The local orientation of the contour of the adjacent polymer m is given by $\theta_j^{(m)}$, which corresponds to the orientation of the polymer segment j of polymer n to which $\Delta \mathbf{r}_{nm}$ connects. Second, if a polymer is interacting with several polymers at a time, we define a weighted average direction of the connecting vectors:

$$\Delta \widetilde{\mathbf{e}}_n := \sum_m C\left(|\Delta \mathbf{r}_{nm}|\right) \frac{\Delta \mathbf{r}_{nm}}{|\Delta \mathbf{r}_{nm}|}. \tag{4}$$

Here $C\left(|\Delta \mathbf{r}_{nm}|\right)$ is a weighting factor accounting for the assumption that a more distant polymer contributes less to an interaction. It is given by

$$C\left(|\Delta \mathbf{r}_{nm}|\right) = \begin{cases} 0 & \text{if } |\Delta \mathbf{r}_{nm}| > d \\ (d - |\Delta \mathbf{r}_{nm}|)/d & \text{else} \end{cases}, \tag{5}$$

where d defines the interaction radius. Using the orientation of the averaged connecting vector $\tilde{\theta}_n$, we define an averaged nematic impact angle as $\Delta \tilde{\theta}_n^{(n)} = \theta_0^{(n)} - \tilde{\theta}_n$. Equipped with these definitions we are now in a position to write down the alignment potential as

$$\tilde{H}_0^{(n)} := \frac{\alpha_n v_0}{d} \cos(2\Delta \tilde{\theta}_n^{(n)}) |\Delta \widetilde{\mathbf{e}}_n|, \tag{6}$$

where the overall amplitude of the alignment is set by the absolute value of the weighted connecting vector, combined with the nematic alignment strength α_n.

The repulsion force $\mathbf{F}_{\mathrm{rep}}$ in Eq. (1) is given by

$$\mathbf{F}_{\mathrm{rep}} = -s \sum_m C\left(|\Delta \mathbf{r}_{nm}|\right) \frac{\Delta \mathbf{r}_{nm}}{|\Delta \mathbf{r}_{nm}|}, \tag{7}$$

which is used to prevent unphysical aggregation of polymers. It is assumed to be weak with $s = 0.05$. Filaments in actomyosin motility assays are observed to conduct a trailing motion, where the tail of a polymer follows the movement of the tip (1, 3–6). To emulate this behaviour, tail joints move according to

$$\partial_t \mathbf{r}_j^{(n)} = K_s \left(\left|\mathbf{r}_j^{(n)} - \mathbf{r}_{j-1}^{(n)}\right| - b\right) \frac{1}{2} \left(\mathbf{u}_{j+1}^{(n)} + \mathbf{u}_j^{(n)}\right). \tag{8}$$

Here, the second part of the equation, $\frac{1}{2}(\mathbf{u}_{j+1}^{(n)} + \mathbf{u}_j^{(n)})$, ensures the movement to be in the direction of the average of the segment's orientations that are adjacent to joint j. The remainder of Eq. (8) corresponds to a linear (Hookian) restoring force with spring coefficient $K_s = 200$ that ensures an average length b of the cylindrical segments between bonds.

Supplementary Note 2: Onset of nematic patterns

In this section we provide further information on how the phase diagram shown in Fig. 1(c) of the main text was obtained.

To determine the density ρ_n as a function of L_p above which nematic patterns are formed, we performed exploratory simulations in the phase space spanned by the (reduced) global polymer density $\langle \rho \rangle L^2$ and the persistence length L_p. To guarantee that the dynamics has reached a steady state we ran these simulations for a time $15\,873$ which is much larger than the initial timescale $t_0 \approx 100$ it takes for a system to reach the quasi-stationary, disordered state (2). Figure S1 shows the results of the *in silico* parameter scans in density at a set of fixed values for L_p: The blue triangles and red squares correspond to steady states where we visually observed nematic patterns or a disordered state, respectively. To determine the phase boundary $\rho_n(L_p)$ we fitted a function $f_\rho(L_p) = a/L_p$ (with a as free fitting parameter) to the data points with the lowest density that still exhibited nematic order [solid line in Fig. S1].

The shape of the boundary line is dictated by the interplay between two counteracting effects: density-dependent, interaction-induced ordering and rotational diffusion. The former increases linearly with density increase, and above the critical value of density, spontaneous ordering begins to predominate over diffusion. Thus, the critical density is proportional to rotational diffusion coefficient and therefore $\propto L_p^{-1}$ in our case. We take $f_\rho(L_p)$ as an approximation to the density corresponding to the onset of nematic patterns, $\rho_n(L_p)$.

To further test whether this is a satisfactory approximation for the phase boundary, we ran ten independent simulations at a density corresponding to ρ_n [cf. dots in Fig. 1 (c) of the main text] and further ten at $0.9\,\rho_n$ for several different L_p for a twice as large simulation time of $31\,746$. All simulations at ρ_n formed ordered patterns, while none at $0.9\,\rho_n$ did, affirming that $f_\rho(L_p)$ adequately approximates the position of the isotropic-nematic transition.

Supplementary Note 3: Defect detection

In this section, we explain the algorithms we used to identify topological defects in simulations of both the hydrodynamic theory and the agent-based model.

To algorithmically detect $-1/2$ defects in both approaches, we took advantage of the fact that inside a defect core the topological charge density q, defined as (7)

$$q = \frac{1}{4\pi} \left(\partial_x \hat{Q}_{xa} \partial_y \hat{Q}_{ya} - \partial_x \hat{Q}_{ya} \partial_y \hat{Q}_{xa}\right), \tag{9}$$

has a very large negative value (with $\hat{Q} = Q/\rho$ and Q defined as in Eq. (11)), whereas in other regions of space its absolute value is much smaller (cf. lower right pane of Fig. 2(a) and (d) of the main text). We exploit this fact and define any contiguous region of space in which q falls below a certain threshold value q_{thrs} as one $-1/2$ defect.

The position of $-1/2$ defects in the *agent-based model* is obtained in the following way. Please first note that the main purpose of the data from the agent-based simulations in Fig. 3(c)-(e) is to qualitatively confirm the trend observed in the hydrodynamic model. To quantify the data with a high degree of precision would require averaging over large ensembles, which would be numerically prohibitively demanding given the very long time scales on which the observed phenomena occur.

The total runtime of each simulation was $142\,857$ (which is much longer than the dynamics of undulations; cf. Movie S1 and S2), from which we cutted an initial transient (cf. section S7) before starting the measurement. For each value of $L_p/\langle \phi \rangle$ we averaged over ten independent simulations.

To obtain q in agent-based simulations, we rasterized space into a grid with a grid spacing of $\Delta x = 0.3$, which is small enough to resolve the structure of a defect (note that the qualitative agreement between the agent-based simulations and hydrodynamic model, shown in Fig. 3 of the main text, does not depend on the exact choice of this and the following numerical parameters). We used the orientations $\theta_0^{(n)}$ of polymer tips residing inside each grid point at a given time to calculate a local value of $\hat{Q}$ using Eq. (11). To suppress noise due to stochastic particle fluctuations, we further averaged over a time span of 15.9, which is much shorter than density rearrangements due to bending undulations. With this we obtained $q(\mathbf{r}, t)$ using Eq. (9). We chose $q_{\text{thrs}} = -0.032$, which is much lower than typical values of q outside defects. Additionally, to avoid classifying small and short-lived density peaks that occur sporadically in the simulations as CTDs, we heuristically filtered them out by requiring the charge density to be below q_{thrs} for a time of at least 159 for a CTD to be detected.

The *hydrodynamic model* allows by construction a direct access to the Q-tensor, which allows a direct calculation of the function q, given by Eq. 9. The positions of $-1/2$ defects are defined as local minima of the function q and, for consistency, the same value of q_{thrs} is used as for the agent based simulations. For the measurements in the hydrodynamic model, we discarded the data collected in the first half of the simulation runs in order to avoid any influence of initial transients. To generate the data shown in Fig. 3 (a), we classified all runs in which CTDs were detected to be CTD-dominated (blue dots in Fig. 3 (a)). Distinction between FAEs and stable bands was made via visual inspection.

Supplementary Note 4: Flux measurement through defects

In the main text, we studied the mass flow through a defect as well as the speed of particles during a CTD passage; see Figs. 4(b) and 4(e), respectively. To this end, we needed detailed information about the position and velocity of particles as they transitioned from one arm of a defect to another. To determine these quantities, we leveraged the possibility offered by the agent-based simulations to access the position of each individual polymer at any given point in time.

In order to be able to deduce that a given polymer has transitioned from one arm of a defect to another one, several things have to be known.

First, one has to find a criterion which allows to algorithmically determine if a polymer is pertinent to a given arm at a given time. For this we used the following heuristics: Over each arm of a defect we placed a round "classification area", which is large enough to cover the full width of the nematic lane (blue regions in Fig. S2, diameter $22\,L$). The positions of the classification areas were chosen such that they roughly coincided with the area where the nematic lanes recovered their full width (midpoint distance of classification areas to defect: $26\,L$ in Fig. S2). Every polymer being inside one of these regions is classified as pertinent to the given defect arm.

Second, one has to find a criterion that allows to make a determination as to the origin of particles that have been classified as belonging to a particular arm. For this we introduced an additionally classification area which encompasses all parts of the simulation box being further away from the defect core than a specific distance, cf. orange region in Fig. S2 (distance to defect: $40\,L$). (Note that the black colored area does not pertain to any classification area.) After this partitioning, we measured the currents from one region to another with the below described heuristics. We did this for a time span sufficiently long enough that many particles can travel from one blue region to another blue region (cf. Fig. S2), but short enough such that bending undulations do not change the position of the individual lanes significantly. Data in Fig. 4(b) averaged over 159, Fig. 4(e) averaged over $4\,019$ trajectories in a time of 317.

For the flux measurement heuristics, we each assigned a unique identifier id to every classification area. We then checked in short intervals of 0.16 for every polymer i if its position coincided with one of the classification areas. If this was the case, polymer i was assigned the identifier of the region and the time of assignment t_{assign} was saved. If polymer i already had a different identifier id' assigned (and hence also a different t'_{assign}), this meant that it had traveled from another classification area into the current region (without crossing a third region in the meantime). In such a case, we stored the pairs of tuples $(id', t'_{\text{assign}})$ and (id, t_{assign}), which allow (combined with with the also saved information of the position and speed of every polymer at every interval) to reconstruct the path polymer i has taken propagating from region id' to id. Subsequently, we replaced the assigned identifier and assignment time of polymer i with that of the current region and the current time and continued the simulation.

Supplementary Note 5: Dispersion in the polymer velocity

Most studies of active matter assume the speed of agents to be constant and uniform (8). Yet, experiments of the actin motility assay show actin filaments to have a broad distribution of velocities (1). To take into account the effects of such a velocity dispersion, we drew the assigned speed of polymers from a distribution (cf. Section S1 of this Supplemental Material). We have found that the introduction of such a velocity dispersion does not hinder the formation of nematic lanes. To additionally check whether particles that possess different free velocities behave differently on the level of macroscopic structures—for example by causing an effective sorting of particles into spatially separate populations, where only relatively fast/slow particles form part of patterns—we subdivided the system into a grid with a grid spacing of $\Delta x = 0.3$ and determined for each grid-cell

the locally averaged $\langle v^{(n)} \rangle$ of particles inside a simulation exhibiting nematic lanes and CTDs. Any local accumulation of fast/slow particles would lead to a different value of $\langle v^{(n)} \rangle$ when compared to the global average $\langle v^{(n)} \rangle_{\text{glob}}$. As can be inferred from Fig. S3, the system is well mixed (up to random fluctuations) with respect to polymer velocities. We further found that the introduction of a velocity dispersion prevented the decay of purely nematic patterns into oppositely propagating polar waves (cf. Ref (1)), which hence seems to be an artefact of the assumption of equal and uniform velocities.

Supplementary Note 6: Width of nematic lanes

As discussed in the main text, we measured the width of nematic lanes as a function of density $\langle \phi \rangle$ in both the agent-based simulations and the hydrodynamic model (at a constant system size). To this end, we performed several simulations at different polymer densities but at a fixed persistence length (resp. several realizations of the hydrodynamic model at different $\langle \phi \rangle$ and fixed λ). After these systems had reached a configuration in which they exhibited a single straight lane, we measured the width of the band and the average density $\langle \phi \rangle_{\text{bg}}$ in the disordered background. (The width is determined by averaging the density of the system along the axis of the straight lane, which results in a one dimensional density profile. The width of the lanes in the hydrodynamic model is then defined as the distance between the two points with the maximal gradient of this curve, which can easily be obtained due to the absence of noise. In the agent based simulations the lane width is heuristically defined as the width of the region where this profile exceeds the threshold of three times $\langle \phi \rangle_{\text{bg}}$.) As shown in Fig. S4, the thickness of the lanes grows linearly with density in both the agent-based simulations and hydrodynamic model, while the density of the disordered background remains constant.

Supplementary Note 7: FAE detection

In this section we describe the procedure we used to measure the mean number of FAEs present at different parameter regimes in the agent-based simulation (Fig. 3(e) of the main text).

For this we logged the formation of every FAE in the investigated systems; the most reliable method for detecting FAEs turned out to be manual inspection of simulation videos. To obtain the mean number of FAEs present, we divided the total lifetime of all detected FAEs in the system by the total observation time. For every investigated L_p in the agent-based simulations, we averaged over ten independent simulations, which each ran for a time of $142\,857$.

It is worth to note that agent-based simulations started in a parameter regime in which systems predominantly exhibit FAEs or stable lanes (i.e., high L_p; see also section "From CTDs to FAEs and bands" in the main text), do not immediately form straight lanes at the onset of pattern formation, but frequently at first dwell in a state of high activity (cf. left panel of Fig. 3(b) in the main text) in which no FAE can develop. We measured the duration of this initial transient ("dwell-time") and found that it is shorter than a time of $70\,000$ in more than ninety percent of the cases.

We discarded this initial time span in the measurements of the mean numbers of CTDs (cf. section S3) and FAEs present to rule out any influence of the initial transient on the results.

Further, we studied the temporal evolution of filamentous arc ejections. The motion of a separating arc in the agent based and the hydrodynamic model, can be visualized using a kymograph of the density projection shown in Fig. S5. As can be inferred from the bending of the lateral extrusions, the separation process of the arcs starts slowly and continues to accelerate until complete ejection and eventual dissolvement of the arc.

Supplementary Note 8: Hydrodynamic model

To provide the motivation of our hydrodynamic model we start form the general form of the evolution equation for the probability distribution function $P(\mathbf{r}, \theta, t)$:

$$\partial_t P(\mathbf{r}, \theta, t) = -L_p \partial_i \big[n_i P(\mathbf{r}, \theta, t) \big] + \partial_\theta^2 P(\mathbf{r}, \theta, t) + \text{interactions}, \tag{10}$$

where $\mathbf{n} = (\cos\theta, \sin\theta)$ is director vector, and L_p is the path persistence length of the polymers. Time is measured in units of the diffusion coefficient. Note that we only consider rotational diffusion and neglect translational diffusion. In the following the space and time dependencies of the probability density are suppressed for brevity. Contribution from the interaction between the polymers can be introduced in the form of collision intergrals in the Boltzmann ansatz (9–12), or by using the gradient of the interaction-induced current in a Smoluchowski approach (13).

We define the particle density ρ, the polarity vector $\mathbf{p}$, and the nematic Q-tensor as the first three moments of the probability distribution function:

$$\rho := \int_0^{2\pi} d\theta \, P(\theta), \qquad p_i := \int_0^{2\pi} d\theta \, n_i P(\theta), \qquad Q_{ij} := \int_0^{2\pi} d\theta \, (2 n_i n_j - \delta_{ij}) P(\theta), \tag{11}$$

4

where the subscripts i and j denote the Cartesian components and δ_{ij} represents the Kronecker delta. It is convenient to consider Fourier harmonics of the probability distribution function:

$$P(\mathbf{r},\theta) = \sum_{k=-\infty}^{\infty} P_k(\mathbf{r})e^{ik\theta}. \tag{12}$$

According to their definitions, ρ, p_i, and Q_{ij} can be expressed via Fourier harmonics as follows:

$$\rho = 2\pi P_0\,, \tag{13a}$$

$$p_i = \pi\big((P_1 + P_{-1}), i(P_1 - P_{-1})\big)\,, \tag{13b}$$

$$Q_{ij} = \pi\big((P_2 + P_{-2}), i(P_2 - P_{-2})\big)\,, \tag{13c}$$

where the symbol i denotes the imaginary unit.

By introducing the projection onto the mth harmonics of P:

$$\overline{(\dots)}^m := \frac{1}{2\pi}\int_0^{2\pi} d\theta\, e^{-im\theta}(\dots)\,, \tag{14}$$

one obtains the following contributions from the advective and diffusive parts of Eq. (10) to the evolution equations of the m_{th} Fourier harmonics (P_m):

$$\partial_t P_m = -m^2 P_m - \overline{L_p \partial_i (n_i P(\mathbf{r},\theta))}^m$$
$$= -m^2 P_m - L_p \frac{1}{2}\left[\partial_x \sum_k P_k(\delta_{k,m-1} + \delta_{k,m+1}) + \partial_y \sum_k P_k(\delta_{k,m-1} - \delta_{k,m+1})/i\right]. \tag{15}$$

In terms of the collective variables this can be rewritten as:

$$\partial_t \rho = -L_p \partial_i p_i\,, \tag{16a}$$

$$\partial_t p_i = -p_i - \frac{L_p}{2}\partial_i \rho + \frac{L_p}{2}\partial_j Q_{ij}\,, \tag{16b}$$

$$\partial_t Q_{ij} = -4Q_{ij} - \frac{L_p}{2}\left[\partial_i p_j + \partial_j p_i - \delta_{ij}\partial_k p_k\right]. \tag{16c}$$

Note, that we imply summation for repeating indices following the Einstein convention. Since we consider a system with purely nematic interactions, the polar order decays on short time scales for all strengths of self-propulsion. Thus, the polarity field $\mathbf{p}$ equilibrates fast and can be eliminated adiabatically to arrive at dynamic equations for the density ρ and Q-tensor alone. We find after rescaling time by a factor of 4:

$$\partial_t \rho = \lambda^2 \Delta\rho + \lambda^2 \partial_i \partial_j Q_{ij}\,, \tag{17a}$$

$$\partial_t Q_{ij} = -Q_{ij} + \frac{\lambda^2}{2}\Delta Q_{ij} + \lambda^2 \left[\partial_i \partial_j \rho\right]^{\text{st}}\,, \tag{17b}$$

where we have introduced the parameter $\lambda := L_p/(2\sqrt{2})$, $\Delta = \partial_i \partial_i$ denotes the Laplace operator, and $[\dots]^{\text{st}}$ indicates the symmetric and traceless part of the expression.

We now discuss the physical meaning of each term on the RHS of Eqs. (17). The first term in the density equation Eq. (17a) acts like effective translational diffusion, despite the fact that it is actually coming from the single particle advection (note, that the real translational diffusion is neglected in our model). The second term in equation Eq. (17a) represents anisotropic flux of material along the nematic order. This term enhances diffusion along the direction of the eigenvector of Q_{ij} corresponding to its positive eigenvalue, and suppresses it along the perpendicular direction. It also can be treated as *curvature-induced* flux, since it disappears in a uniformly ordered state.

The first term in the evolution equation of the nematic tensor Eq. (17b) is due to the thermal rotational diffusion. If there were no interaction between polymers, the action of this term would lead to disordering. The second term in Eq. (17b) penalizes the distortion of Q_{ij} and represents the elasticity in terms of liquid crystal theory. The last term of Eq. (17b) provides the coupling between the equations. It can be treated simply as an anisotropic diffusive contribution. But it also introduces "aligning torque" by changing the orientation of nematic order in the presence of the density gradients.

Finally, besides the diffusion- and advection-related terms we need to add interaction-induced contributions. Inspired by Refs. (14, 15) we also introduce the following terms to describe the nematic interactions of the polymers:

$$\partial_t \rho = \dots + \tilde{\nu}_\rho \Delta\rho^2 + \tilde{\chi}_\rho \partial_i \partial_j (\rho Q_{ij})\,, \tag{18a}$$

$$\partial_t Q_{ij} = \dots + \tilde{\alpha}\rho Q_{ij} - \tilde{\beta}Q^2 Q_{ij} + \tilde{\kappa}_\rho \langle\rho\rangle \Delta Q_{ij} + \tilde{\omega}^a \left[2\partial_i \rho \partial_j \rho\right]^{\text{st}}. \tag{18b}$$

The $\tilde{\nu}_\rho$-related term in Eq. (18a) comes from the excluded volume interactions between the polymers (however an analogous term occurs due to the "collision" of polymers, e.g., see Ref. (14)). The last term in Eq. (18a) is an interaction-induced flux representing a *density-dependant correction* (16) to the last term of Eq. (17a).

The first term of Eq. (18b) promotes density dependent ordering, which competes with motility-induced disordering coming from the fist term of Eq. (17b); β is a non-equilibrium Landau coefficient setting the magnitude of order in the bulk. $\tilde{\kappa}_\rho \langle \rho \rangle$ contributes to the restoring elastic constant. As can be seen, this is the only term in our theory that is linearized around the mean density value, whereas in the most of hydrodynamic models almost all terms in Eq. (18) are subjected to this procedure. We linearize this particular term for two reasons. Firstly, for the sake of simplicity: we want this term to represent one particular effect – elasticity (or "rigidity" in terms of the material). Secondly, with this linearization it's simpler to interpret the term $\tilde{\kappa}_\rho \langle \rho \rangle \Delta Q_{ij}$ as stemming from a free energy, while the contribution $\tilde{\kappa} \Delta (\rho Q_{ij})$ could not be obtained from a free energy. Finally, the last term of Eq. (18b) describes the non-equilibrium anchoring to the density interface (15).

We emphasize again that we are not linearizing $\tilde{\nu}_\rho$, $\tilde{\chi}_\rho$, and $\tilde{\omega}^a$ - related terms around the mean density (the latter of which would simply disappear completely in that case). Such higher-order terms are typically linearized (or ignored) in well-controlled closures in the vicinity of the isotropic/nematic transition (e.g., within Boltzmann–Ginzburg–Landau approach (11, 17–19)). However, our observations hint that this linearization procedure, widely used in the field of active nematics, may result in some physical processes not being accounted for by the resulting models, which in turn can leads to some phenomena (e.g., such as CTDs) escaping the researchers' gaze as well.

To obtain the equations of motion presented in the main text we simply combine Eq. (17) and Eq. (18) and re-normalize density by the critical one $\phi = \rho / \rho_n$. The coefficients are also renamed accordingly: $\tilde{\kappa}_\rho \to \kappa_\phi$, etc.

As discussed in the main text, the hydrodynamic model allows to directly access the direction and magnitude of the anisotropic active flux $-\partial_j (\chi Q_{ij})$. To complement the illustration of this flux in Fig. 4(d) of the main text, we show in Fig. S6 a direct plot of this observable as recorded in the hydrodynamic model.
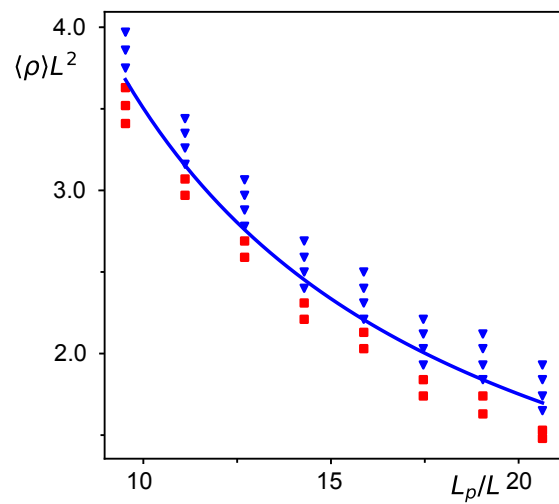
Fig. S1. Phase space of nematic order. Agent-based simulations yielding nematic patterns are marked with blue triangles. Simulations exhibiting no order are shown as red squares. A fit of the functional form $f_\rho(L_p) = a/L_p$, where a is the free fit parameter, to the ordered datapoints with the lowest density is shown in solid blue. (See Appendix for parameters.)
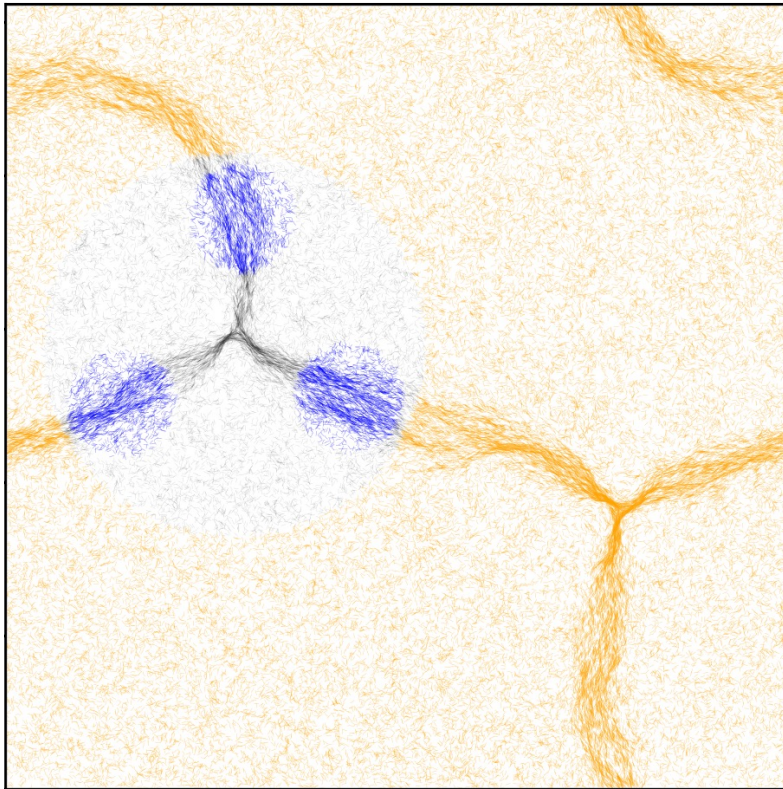
Fig. S2. Illustration of classification areas. Representative spatial domain of an agent-based simulation containing 91217 polymers which exhibits two condensed topological defects (CTDs). A circular classification area (regions where the polymers are colored blue) is placed over each nematic lane that emanates as an arm from one of the defects. Polymers being further away from the defect than the blue classification areas are pooled into one large classification area (shown in orange). All black colored polymers do not belong to any classification area. (Parameters: $L_p = 11L$, simulation box size: $163L$; see Appendix for further parameters.)
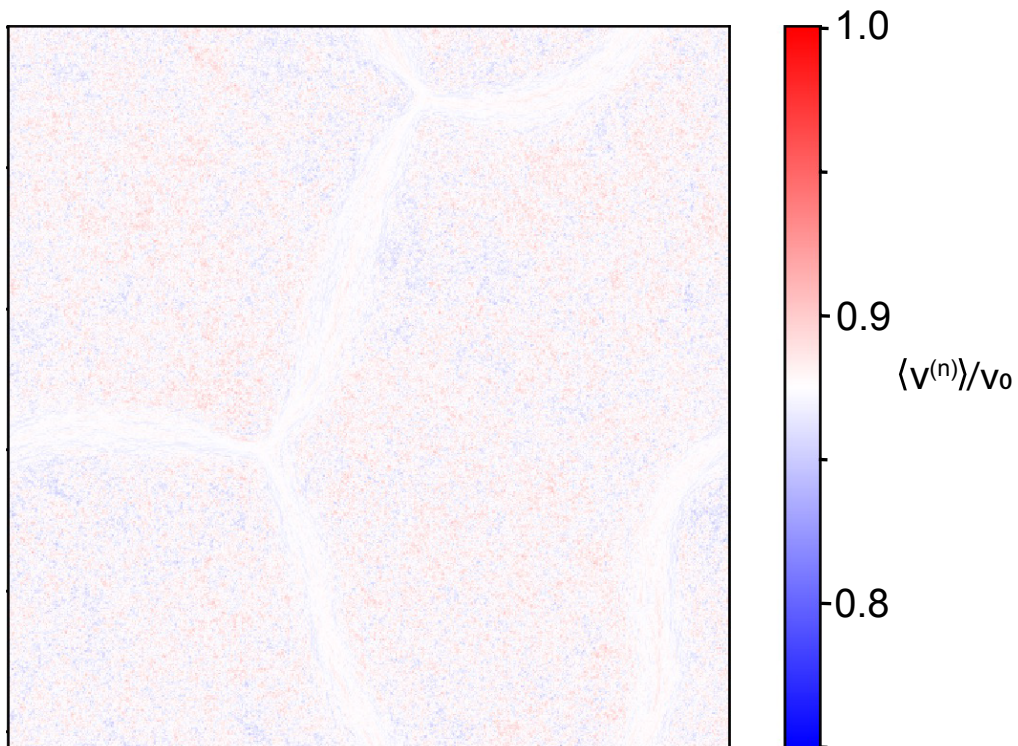
Fig. S3. Local averaged velocities. Local average of the free velocities $v^{(n)}$ of the agents in a system exhibiting nematic patterns. The values of the local averages, $\langle v^{(n)} \rangle$, do not deviate (up to random fluctuations) of the value obtained when averaging over all polymers inside the simulation ($\langle v^{(n)} \rangle_{\text{glob}} = 0.875 v_0$, where v_0 is the maximal speed of a free polymer). Same data and parameters as used in Fig. 2(a) [the position of the patterns is still perceivable since fluctuations in the low density disordered background are less suppressed, due to the lower number of polymers over which is being averaged, compared with the high density nematic lanes.]
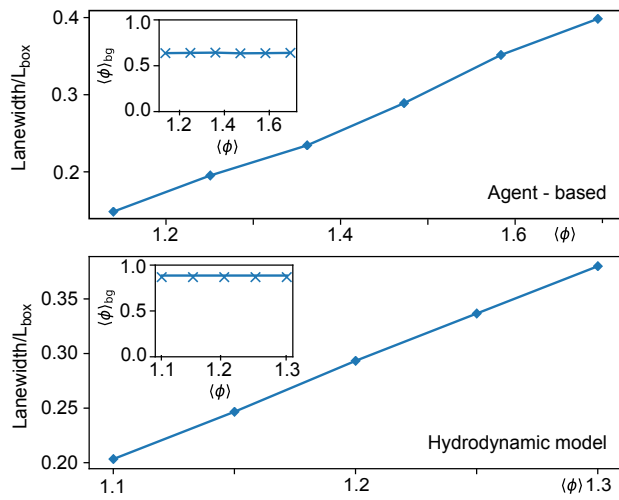
Fig. S4. Width of nematic lanes for agent-based simulations (*upper panel*) and for the hydrodynamic model (*lower panel*). The width of stable nematic lanes grows with an increase of the global density $\langle\phi\rangle$ while the background density $\langle\phi\rangle_{\mathrm{bg}}$ stays constant (inset). Parameters: $L_p = 20.6L$; see Appendix for further parameters.
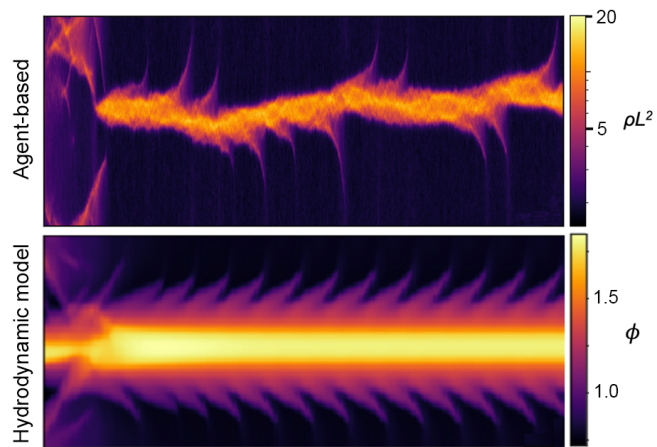
Fig. S5. Temporal evolution of FAEs Illustration of a system exhibiting several filamentous arc ejections in sequence in agent based simulations (*upper panel*) and hydrodynamic model (*lower panel*). The density is projected/averaged along the long axis of the lane. The resulting 1-D slices are stacked into the shown Kymograph. Each FAE can be recognized by an extrusion from the lane. The slight bending of these extrusions towards a more vertical shape is a signature of the accelerated motion of the ejection.
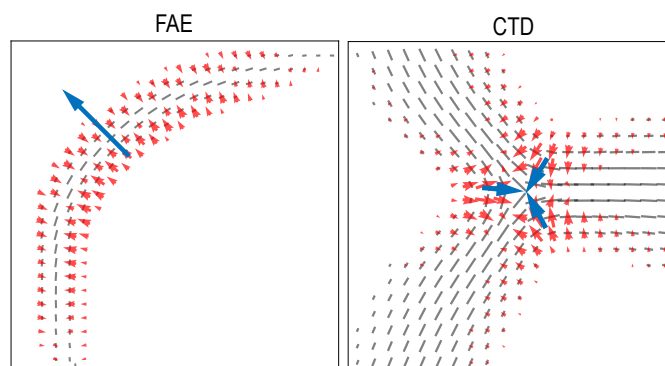
Fig. S6. Anisotropic active flux. Plot of $-\partial_j(\chi Q_{ij})$ in the hydrodynamic model. Grey segments represent nematic order and the red arrows corresponds to the magnitude and direction of the current.

strong "anchoring"   weak "anchoring"
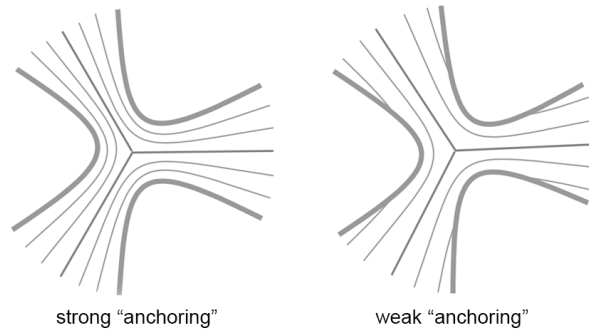
Fig. S7. Anchoring. Depictions of the nematic fieldlines inside a CTD with strong (large $|\omega^\alpha|$) and weak (small $|\omega^\alpha|$) bilinear anchoring term, respectively.

Movie S1

Constantly undulating nematic lanes in an agent-based simulation. (Parameters are: ρL^2=3.15, L_p=11.1. Scale-bar: 15L. Density averaged over a time of 15.9 for better visibility.)

Movie S2

Emergence of a multitude of condensed topological defects in agent-based simulations. Note that the lateral movement of lanes happens on long timescales. A single frame roughly corresponds to the time of 162 a straight moving particle with a velocity of v_0 needs to cross the whole system. (Parameters are: ρL^2=3.2, L_p=11.9. Scale-bar: 15L. Density averaged over a time of 15.9 for better visibility.)

Movie S3

Two condensed topological defects are formed simultaneously in an agent-based simulation. Due to continued undulation of the connecting nematic lanes the defects eventually disintegrate. (Parameters are: ρL^2=3.47, L_p=11.1. Scale-bar: 15L. Density averaged over a time of 3 for better visibility.)

Movie S4

Several filamentous arc ejection develop in succession along a nematic lane in an agent-based simulation. (Parameters are: ρL^2=2.7, L_p=14.3. Scale-bar: 15L. Density averaged over a time of 15.9 for better visibility.)

Movie S5

Straight and stable nematic lane in an agent-based simulation. (Parameters are: ρL^2=1.9, L_p=20.6. Scale-bar: 15L. Density averaged over a time of 15.9 for better visibility.)

Movie S6

Details of a flux in an agent-based simulation from one arm of a condensed topological defect to the two others. The path that is taken by the polymer heads is traced out. Only trajectories that start in the upper left arm and eventually will go to either the lower or upper right arm are visible. (Parameters are: ρL^2=3.5, L_p=11.1.)

Movie S7

Emergence of a multitude of condensed topological defects in a simulation of the hydrodynamic model. (Parameters are: $\beta = 0.05, \kappa_\phi = 0.2, \omega^a = -0.5, \chi_\phi = 0.4, \nu_\phi = 1, \lambda = 1, \langle \phi \rangle = 1.1$)

Movie S8

Several filamentous arc ejection develop in succession along a nematic lane in a simulation of the hydrodynamic model. (Parameters are: $\beta = 0.05, \kappa_\phi = 0.2, \omega^a = -0.5, \chi_\phi = 0.4, \nu_\phi = 1, \lambda = 1.2, \langle \phi \rangle = 1.1$)

Movie S9

Straight and stable nematic lane in a simulation of the hydrodynamic model. (Parameters are: $\beta = 0.05, \kappa_\phi = 0.2, \omega^a = -0.5, \chi_\phi = 0.4, \nu_\phi = 1, \lambda = 1.4, \langle \phi \rangle = 1.1$)

Movie S10

Three-beam symmetrical arrangement of sources of polar particles. The ensuing nematic currents eventually form a condensed topological defect. (Parameters are: ρL^2=3.6, L_p=14.3. Scale-bar: 15L. Density averaged over a time of 15.9 for better visibility.)

Bibliography

1. L Huber, R Suzuki, T Krüger, E Frey, and AR Bausch. Emergence of coexisting ordered states in active matter systems. *Science*, 361(6399):255–258, doi: DOI:10.1126/science.aao5434.

2. Lorenz Huber, Timo Krüger, and Erwin Frey. Microphase separation in active filament systems maintained by cyclic dynamics of cluster size and order. *Phys. Rev. Res.*, 3(1):013280, doi: 10.1103/PhysRevResearch.3.013280.

3. Volker Schaller, Christoph Weber, Christine Semmrich, Erwin Frey, and Andreas R. Bausch. Polar patterns of driven filaments. *Nature*, 467(7311):73–77, doi: 10.1038/nature09312.

4. Tariq Butt, Tabish Mufti, Ahmad Humayun, Peter B. Rosenthal, Sohaib Khan, Shahid Khan, and Justin E. Molloy. Myosin Motors Drive Long Range Alignment of Actin Filaments. *J. Biol. Chem.*, 285 (7):4964–4974, doi: 10.1074/jbc.M109.044792.

5. Saman Hussain, Justin E. Molloy, and Shahid M. Khan. Spatiotemporal Dynamics of Actomyosin Networks. *Biophys. J.*, 105(6):1456–1465, doi: 10.1016/j.bpj.2013.08.001.

6. Ryo Suzuki, Christoph A. Weber, Erwin Frey, and Andreas R. Bausch. Polar pattern formation in driven filament systems requires non-binary particle collisions. *Nat. Phys.*, 11(10):839–843, doi: 10.1038/nphys3423.

7. Matthew L Blow, Sumesh P Thampi, and Julia M Yeomans. Biphasic, lyotropic, active nematics. *Phys. Rev. Lett.*, 113(24):248303, doi: 0.1103/PhysRevLett.113.248303.

8. Hugues Chaté. Dry aligning dilute active matter. *Annu. Rev. Condens. Matter Phys.*, 11(1), doi: 10.1146/annurev-conmatphys-031119-050752.

9. Eric Bertin, Michel Droz, and Guillaume Grégoire. Boltzmann and hydrodynamic description for self-propelled particles. *Phys. Rev. E*, 74:022101, doi: 10.1103/PhysRevE.74.022101.

10. Eric Bertin, Michel Droz, and Guillaume Grégoire. Hydrodynamic equations for self-propelled particles: microscopic derivation and stability analysis. *J. Phys. A Math. Theor.*, 42(44):445001, doi: 10.1088/1751-8113/42/44/445001.

11. Anton Peshkov, Igor S Aranson, Eric Bertin, Hugues Chaté, and Francesco Ginelli. Nonlinear field equations for aligning self-propelled rods. *Phys. Rev. Lett.*, 109(26):268701, doi: 10.1103/PhysRevLett.109.268701.

12. A. Peshkov, E. Bertin, F. Ginelli, and H. Chaté. Boltzmann-Ginzburg-Landau approach for continuous descriptions of generic Vicsek-like models. *Eur. Phys. J.: Spec. Top.*, 223(7):1315–1344, doi: 10.1140/epjst/e2014-02193-y.

13. Aparna Baskaran and M Cristina Marchetti. Nonequilibrium statistical mechanics of self-propelled hard rods. *J. Stat. Mech. Theory Exp.*, 2010(04):P04019, doi: 10.1088/1742-5468/2010/04/P04019.

14. Ivan Maryshev, Andrew B Goryachev, Davide Marenduzzo, and Alexander Morozov. Dry active turbulence in a model for microtubule–motor mixtures. *Soft Matter*, 15(30):6038–6043, doi: 10.1039/c9sm00558g.

15. Ivan Maryshev, Alexander Morozov, Andrew B Goryachev, and Davide Marenduzzo. Pattern formation in active model c with anchoring: bands, aster networks, and foams. *Soft Matter*, 16(38): 8775–8781, doi: 10.1039/d0sm00927j.

16. A. Baskaran and M. C. Marchetti. Self-regulation in self-propelled nematic fluids. *Eur. Phys. J. E*, 35(9), doi: 10.1140/epje/i2012-12095-8.

17. Francesco Ginelli, Fernando Peruani, Markus Bär, and Hugues Chaté. Large-scale collective properties of self-propelled rods. *Phys. Rev. Lett.*, 104(18):184502, doi: 10.1103/PhysRevLett.104.184502.

18. Sandrine Ngo, Francesco Ginelli, and Hugues Chaté. Competing ferromagnetic and nematic alignment in self-propelled polar particles. *Phys. Rev. E*, 86(5):050101, doi: 10.1103/PhysRevE.86.050101.

19. Sandrine Ngo, Anton Peshkov, Igor S. Aranson, Eric Bertin, Francesco Ginelli, and Hugues Chaté. Large-Scale Chaos and Fluctuations in Active Nematics. *Phys. Rev. Lett.*, 113:038302, doi: 10.1103/PhysRevLett.113.038302.